

Metasurface-based Snapshot Shortwave-Infrared Hyperspectral Image Reconstruction with Inter and Intra Prior Learning Network

Linqiang Li, Pan Liu, Haofang Yan, Ziqin Zhang, Jinglei Hao, Seong G. Kong, Yongqiang Zhao *

Abstract—Shortwave-infrared(SWIR) spectral information, ranging from $1\ \mu\text{m}$ to $2.5\ \mu\text{m}$, breaks the limitations of traditional color cameras in acquiring scene information and has been used in many fields. However, conventional SWIR hyperspectral imaging systems face challenges due to their bulky setups and low acquisition speed. In this work, we introduce a snapshot SWIR hyperspectral imaging system based on a metasurface filter and a corresponding filter selection method to achieve the lowest correlation coefficient among these filters. This system has the advantages of small size and snapshot imaging. We propose a novel inter and intra prior learning unfolding framework proposed to achieve high-quality SWIR hyperspectral image reconstruction, which bridges the gap between prior learning and cross-stage information interaction. We also design an adaptive feature transfer mechanism to adaptively transfer contextual correlation of multi-scale encoder features to prevent detailed information loss in the decoder. Experiment results demonstrate that our method can reconstruct HSI with high speed and superior performance over existing methods.

Index Terms—Hyperspectral imaging, Metasurface, Shortwave infrared, Deep learning, Snapshot compressive imaging.

I. INTRODUCTION

Hyperspectral imaging(HSI), characterized by spatial-spectral data-cube, offers rich spectral information that can be beneficial in various fields such as medical diagnosis [1], [2], food safety [3] and remote sensing [4], [5]. Conventional hyperspectral imaging systems typically involve temporal sequential scanning of either the spatial [6], [7] or spectral [8] domain. However, such temporal scanning procedure result in slow imaging processes that are unsuitable for dynamic or real-time applications. Recently, Snapshot Compressive Imaging (SCI) systems like coded aperture snapshot spectral imaging (CASSI) [9]–[11] and broadband filter imaging [12], [13] provides an elegant solution, These systems utilize a 2D detector to capture a 3D hyperspectral cube in a single and reconstruct the HSI based on compressed sensing principles. As shown Fig 1.(a), CASSI spatially modulates the 3D HSI with a coded aperture and spectrally shifts it with a dispersive elements. The data captured by the sensor actually is an aliasing of different of monochromatic images. However, the use of complex optical components has made these systems relatively large and not easily portable or integrated with mobile devices.

Unlike CASSI, broadband filter imaging systems directly modulate spectral information through the platforms that

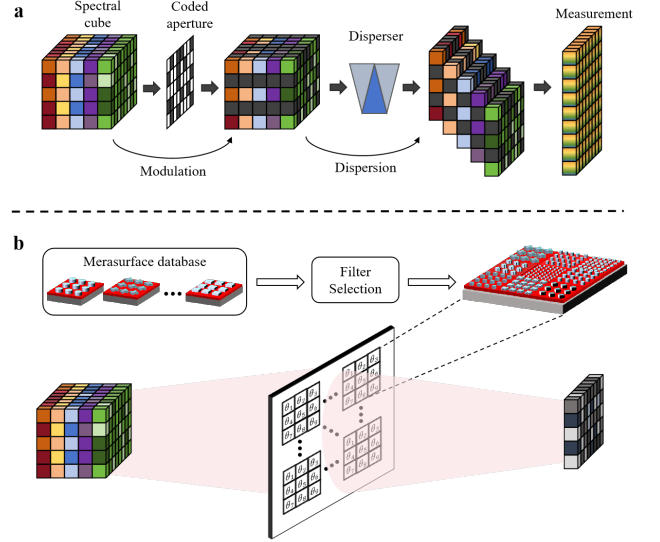


Fig. 1. Schematic representation of different snapshot compressive imaging system. a: The architecture of CASSI system; b: Our snapshot SWIR hyperspectral imaging system based on metasurface filter.

composed of basic filter patterns and integrated with sensor as shown in Fig 1.(b). In such a architecture, the layout of apertures and disperses is no longer required. Xiong *et al.* [14] first proposed a silicon real-time spectral imaging chip in visible band. He *et al.* [15] extended metasurface-based snapshot imaging systems into the near infrared(NIR) range of $0.7\text{--}1\ \mu\text{m}$, and designed a meta attention network to achieve HSI reconstruction. However, these studies neglect spectral imaging in shortwave infrared(SWIR) range of $1\text{--}2.5\ \mu\text{m}$, which indeed is significant in gas detection, standoff imaging, and material detection.

Additionally, the reconstruction quality of SCI systems heavily depends on filter selection and reconstruction algorithm. Existing methods have shortcomings in two aspects. The randomness of basic filter patterns is crucial for spectral coding efficiency and meeting the conditions for compressed information reconstruction. However, exhaustive search methods and the evolutionary optimization methods [16] require multiple spectral reconstructions to verify the effectiveness of selected filters, making them extremely slow. Correlation-based methods [14], [15] lacks efficient optimization processes for selecting optimal filter pattern with the lowest correlation.

Existing algorithms for HSI reconstruction can be cate-

*Corresponding author

gorized into three main types: traditional model-based approaches, deep learning-based approaches and deep unfolding network methods. Traditional model-based methods [17]–[20] address an ill-posed optimization problem iteratively using manually designed prior. While these methods offer high interpretability, they are constrained by the limitations of hand-crafted priors and exhibit slow reconstruction speeds. Deep learning-based methods [21]–[24] leverage the nonlinear mapping ability of deep networks to directly learn a mapping from 2D measurements to 3D hyperspectral cubes, leading to significant advancements in reconstruction quality and speed. However, they lack explicit representation of the imaging mechanism and process HSI reconstruction as a black-box, which limits its further improvement. Deep unfolding networks (DUNs) [25]–[31] address the challenge of limited interpretability in black-box networks by combining deep learning with mathematical models. They execute the iterative process using a gradient descent module and enhance the intermediate output through a deep prior module. Although existing DUNs address certain limitations of model-based and learning-based methods, there remain several challenges. Firstly, several works utilize deep prior modules to learn HSI’s implicit priors to guide spectral reconstruction, such as low rank [32], Gaussian mixture models [33], and deep subspace projection [34], etc. However, the knowledge prior acquired by each individual prior module cannot be effectively shared throughout the multi-stage optimization process, resulting in sub-optimal of prior learning. Secondly, skip feature interaction between the encoder and decoder of U-Net can effectively decrease information loss caused by up- and down-sampling operations. But existing works use simple skip residual concatenation [27], [35], which cannot complement detailed features of HSI, while rough multi-scale feature fusion [36] may introduce additional noise.

In this paper, we propose a novel filter selection method for simulating a metasurface-based snapshot spectral imaging system in the shortwave infrared (SWIR) range of 1–2.5 μm and a corresponding deep unfolding network-based algorithm to achieve HSI reconstruction. For the imaging system simulation, we consider sufficient spectral variety and high transmission, designing thousands of metasurface units constructed by silicon nanopillars. Then we obtain the optimal basic filter pattern with our proposed optimization schedule, ensuring the lowest mutual correlation between units. Ablation studies demonstrate that our proposed filter selection procedure significantly benefits reconstruction quality a lot. In terms of the reconstruction algorithm, we propose a novel inter&intra prior learning network with a high performance. To achieve global prior learning in deep unfolding network, we introduce a query prior to interact with each stages and learn HSI’s low rank prior. Considering the information loss between encoder and decoder, we design an adaptive feature transfer module to construct contextual correlation features of different scales and transfer them into the decoder.

The contributions of this paper can be summarized as follows:

- Proposes a novel filter selection method for sufficient coding of incident spectrum and satisfactory of compressed

information reconstruction is proposed to construct a metasurface-based SWIR snapshot spectral imaging system.

- Proposes a novel inter-stage prior learning and intra-stage feature transfer deep unfolding network (ERRA) for HSI reconstruction is proposed.
- Introduces an elegant cross-stage low-rank prior learning module is introduced to learning HSI’s low-rank prior across stages.
- Introduces an efficient adaptive feature transfer module is introduced to effectively transfer contextual correlation knowledge from the encoder to the decoder.

The rest of paper is organized as follows. In Section II, we reviews related work. In Section III, we describes the details of the proposed pattern optimization and HSI reconstruction algorithm. In Section IV, we conduct comprehensive experiments and ablation studies. In Section V presents the conclusion.

II. RELATED WORK

Pattern Optimization Arad and Ben-Shahar [16] first identified that the accuracy of HSI reconstruction was heavily dependent on the selection of filter pattern and proposed an evolutionary optimization to select the optimal filter pattern. However, it requires training the HSI reconstruction network multiple times. Cui *et. al* [14] the utilize inner product of filter spectral response (FSR) to measure mutual correlation in the pattern, They set initial units from the entire metasurface database and optimize the pattern by replacing units that exceed the correlation upper threshold. Although this avoids redundant training processes, it still requires thousands of iterations. He *et. al* [15] use the correlation coefficient as a measurement and strive to minimize the average correlation in the whole pattern, but it still lack a simple and effective optimization procedure, resulting in non-uniformity of mutual correlation coefficients in the array.

Model-based Methods. Traditional methods solve the inverse problem of spectral reconstruction by modeling a system of linear equations. The target spectrum can be effectively reconstructed by utilizing prior knowledge as regularization terms such as total variation [37], dictionary learning [38], [39], non-local low rank [40], [41], and Gaussian mixture models [42]. In several studies, sparse optimization-based methods, which rely on the assumption of HSI’s sparsity as prior and use l_1 to regularize the solution, have demonstrated better performance in reconstruction quality. In [43], a Gaussian kernel-based sparse transform is proposed to solve reconstruction problem of specific mapping. [44] performs over-complete dictionary learning on HSI, then solves least square regression with sparse regular terms. This combination of dictionary learning and sparsity regularization has been widely used in HSI imaging of broadband filter arrays.

However, these method cannot bridge the gap between hand-crafted prior and real-world spectra, resulting in instability in the reconstruction results. The iterative process takes too long, making it difficult to meet the needs of real-time imaging.

Deep Learning-based Methods. Depending on the representation ability of neural networks, deep learning-based HSI reconstruction methods have attracted widespread attention in recent years. The pioneering method [45] used convolutional neural networks to extract the spectral correlation between local pixels for spectral reconstruction. Stiebel *et al.* [46] introduced U-Net [47] to further mine non-local similarity and multi-scale detailed features. Subsequently, many variants of convolution-based spectral reconstruction models were derived [48], [49]. Later, TSA-Net [21] stacked spatial-spectral transformers to reconstruct HSI. BIRNAT [50] integrated the expressive power of an end-to-end convolutional framework with the sequence correlation extraction capability of bidirectional Recurrent Neural Networks (RNNs) for HSI reconstruction. To further improve the efficiency of Transformer for compressive sensing problems, CST [10] and MST [11] were proposed to reform the attention mechanism to reveal intrinsic characteristics of HSI and reduce computational and memory costs.

Although high quality and real-time reconstruction have been achieved, these brute-force methods lack interpretability and fully utilization of transmittance characteristics.

Interpretable network Methods. Commonly used optimization algorithms for HSI reconstruction, such as HQS [51], ADMM [52], PGD [53], GAP [54], can be disentangled into data fidelity and regularization terms, leading to iterative optimization algorithms that alternately solve the data subproblem and the prior subproblem. Interpretable network methods usually solve the prior subproblem as a denoising subproblem while retaining data subproblem, combining the interpretability of model-based method and the strong generalization ability of deep-learning-based methods. Plug-and-play methods [55], [56] first leveraged pre-trained neural networks that have learned from extensive spectral data to enhance reconstruction accuracy in both spatial and spectral domains. Although such method shows strong generalization ability and are free from pre-training, they still face the challenge of being time-consuming due to the iterative gradient descent procedure.

Apart from Plug-and-play methods, deep unfolding networks unfold deep networks and insert data fidelity term into the training process, thus achieving joint optimization. For instance, ADMM-Net [28] unfolded the alternating direction method of multipliers with a convolutional neural network. DSSP [57] extended the half-quadratic splitting (HQS) method and created a spatial-spectral deep prior to enhance the data fidelity. DGSMP [25] presented an unfolding model estimation framework that utilizes the learned Gaussian scale mixture prior to enhance the model's performance. RDLUF [36] introduces interaction between different stages with a sequence feature learning formula (similar to GRU [58]), Song *et al.* [59] implemented feature interaction between different stages using a channel self-attention mechanism, and replaced the process of combining inertia and original gradient terms with an adaptive network.

Although the above methods attempt image prior learning or information interaction between different stages, they still separate the two problems, and never try to solve them in the same module. Additionally, existing methods neglect efficient

feature transfer from encoder to decoder stages, which is crucial for retaining detailed features.

III. METHOD

A. Filter selection

As shown in Fig 1.(b), the metasurface-based SWIR snapshot imaging system integrates an imaging plane onto a sensor plane. The imaging plane $\Theta \in R^{H \times W \times \lambda}$ comprises a set of metasurface-based basic filter patterns made of Si and fabricated on a SiO_2 substrate. These patterns consists of 3×3 different spectral filters obtained through our proposed filter selection method. Each spectral filter is constructed using the same metasurface units arranged in a regular layout.

Under such a design, each filter with random peaks captures a portion of spectral information in a local area (ie: 3×3 pixels), while each pixel is also influenced by additional information from surrounding pixels. Additionally, we apply a compressed sensing-based algorithm in combination with deep learning to achieve HSI reconstruction, which requires optimizing the metasurface's transmission spectra according to compressed sensing principles. Based on the above two points, the filter selection must meet the criteria of minimizing coefficient correlation to effectively encode incident spectrum and adhere to the Restricted Isometry Property (RIP) for accurate compressed information reconstruction.

We design thousands of meta units and removal units with limited randomness under a constraint of transmittance curve gradient threshold. This pre-processed set of metasurface units is utilized as a metasurface dataset $M \in R^{N \times \lambda}$ for filter selection.

Algorithm 1 Filter selection.

- 1: **Input** :Entire Metasurface Dataset $M \in R^{N \times \lambda}$
 - 2: **Output** :Selected Metasurface $\theta \in R^{9 \times \lambda}$
 - 3: **Preprocess**
 - 4: $\mu_i = \frac{\sum_{k=1}^{\lambda} M[i,k]}{\lambda} \leftarrow$ mean of transmission spectra
 - 5: $\sigma_i^2 = \frac{\sum_{k=1}^{\lambda} (M[i,k] - \mu_i)^2}{\lambda} \leftarrow$ standard deviation
 - 6: $cov[i, j] = \frac{\sum_{k=1}^{\lambda} (M[i,k] - \mu_i) \times (M[j,k] - \mu_j)}{\lambda} \leftarrow$ covariance
 - 7: $p[i, j] = \frac{cov[i, j]}{\sigma_i \times \sigma_j} \leftarrow$ pearson correlation coefficient
 - 8: $d \leftarrow$ initialized coefficient in R^N
 - 9: $index = \min_index(\frac{\sum_{j=1}^N |p[i, j]|}{N-1}) \quad i \neq j$
 - 10: $\theta[1] = index$
 - 11: **for all** $i = 2, \dots, 9$ **do**
 - 12: $mask = p[index] > d$
 - 13: $d[mask] = p[index, mask]$
 - 14: $index = \min_index(d)$
 - 15: $\theta[i] = index$
 - 16: **end for**
-

Inspired by the farthest point sampling algorithm, we first calculate the coefficient correlation between units and select

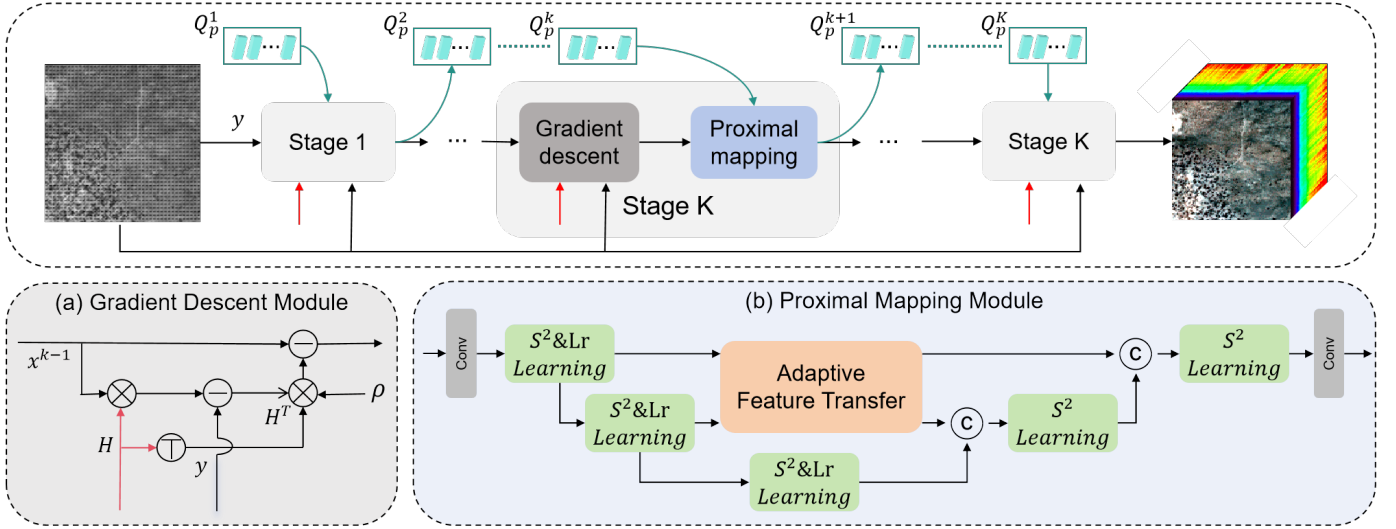


Fig. 2. Illustration of the proposed ERRA for HSI reconstruction, Top: the overall architecture that consists of K stages, each of them which consists of a gradient descent module and a proximal mapping module. (a) Gradient descent module; (b) Proximal mapping module.

the metasurface with the lowest total correlation as a reference structure. Then, we search for units with the least correlation to the the reference structure within M as a new structure. We repeat these steps until 9 units are selected, denoted as $\theta \in R^{9 \times \lambda}$ as described in Algorithm 1.

B. Reconstruction problem formulation

Considering a HSI $X \in R^{H \times W \times \lambda}$, the captured HSI from target scenes is modulated via Θ , and the measurement $Y \in R^{H \times W}$ on sensor plane is denoted as:

$$Y = \Theta \cdot X + n \quad (1)$$

where \cdot denotes the element-wise multiplication, $n \in R^{H \times W}$ represents additive noise in the coding process. HSI reconstruction aims to recover high-quality image X from its measurement Y , which is typically an ill-posed problem.

Mathematically, the solution of HSI reconstruction could be modulated as:

$$x = \operatorname{argmin} \frac{1}{2} \|y - \Theta x\|_2^2 + \lambda \phi(x) \quad (2)$$

the first term is data fidelity term, while the second term ϕ is regularization term. λ denotes a regularization parameters.

In the iterative shrinkage thresholding algorithm (ISTA), Eq. 2 expressed as an iterative convergence problem through the following iterative function:

$$r^{(k)} = x^{(k-1)} - \rho \Theta^\top (\Theta x^{(k-1)} - y), \quad (3)$$

$$x^{(k)} = \operatorname{argmin} \frac{1}{2} \|x - r^{(k)}\|_2^2 + \lambda \phi(x), \quad (4)$$

where k denotes the number of ISTA iteration and ρ denotes the step size. The Eq. 3 is a gradient operation and Eq. 4 can be solved by proximal mapping as following:

$$x^{(k)} = \operatorname{prox}(r^{(k)}) \quad (5)$$

The ISTA algorithm iteratively updates $r^{(k)}$ and $x^{(k)}$ until convergence, but it mainly suffers from two problems. Firstly, the manually designed weight parameter has poor generalization ability, resulting in low fidelity of reconstructed HSI. Secondly, it requires pixel-by-pixel spectral reconstruction, thus the reconstruction time sharply increases with the increase in spatial resolution. To address these issues, we unfold the ISTA algorithm and integrate our designed network into the gradient descent step.

C. Proximal mapping network

Fig.2 presents the whole architecture of our proposed ERRA for HSI reconstruction, which is composed of K stages to reconstruct a coded HSI. In each stage, a gradient descent module is followed by a proximal mapping module; The former aims to utilize transmittance information while the later is for optimization. Our proximal mapping module adopts a three-level U-shaped structure built using basic $S^2 \& L_r$ prior learning block. The proximal mapping module uses a $\operatorname{conv} 3 \times 3$ to map the output feature of upper layer $X_{k-1} \in R^{H \times W \times \lambda}$ into feature $X_0 \in R^{H \times W \times C}$. X_0 passes through the encoder, bottleneck and decoder to be embedded into deep feature $X_d \in R^{H \times W \times C}$. Each level of the an encoder contains an $S^2 \& L_r$ prior learning and a downsample module, while the decoder contains an upsample module and an S^2 prior learning module. Finally, a 3×3 convolution operates on X_d to generate output image $X_k \in R^{H \times W \times \lambda}$. We also introduce an adaptive feature transfer block, which dynamically transfers detailed and high-frequency features from the multi-scale encoder to the decoder.

$S^2 \& L_r$ Prior Learning Block The $S^2 \& L_r$ prior learning block plays an important role in realizing prior learning. It consists of two layer normalization steps, a spatial-spectral prior learning branch, a low-rank prior learning branch in a parallel design, and a feed-forward network, as shown in Fig. 3 (f). The down-sampling module comprises a maxpool

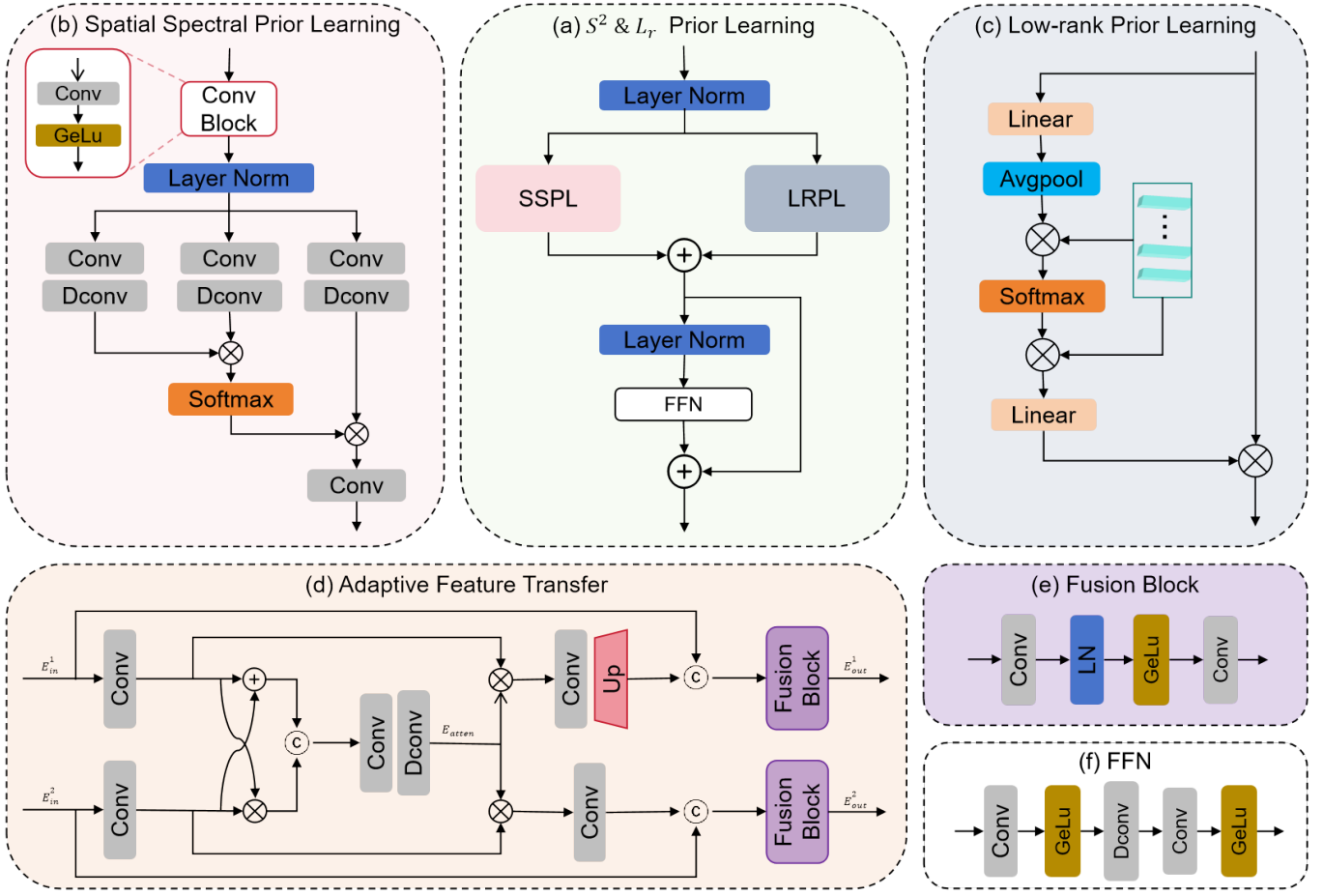


Fig. 3. Diagram of the $S^2 \& l_r$ Prior Learning. (a) The basic unit of the $S^2 \& l_r$ Prior Learning Block; (b) The structure of the spatial spectral prior learning branch; (c) The structure of the low-rank prior learning branch; (d) The structure of the adaptive feature transfer block; (e) The component of the Fusion block; (f) The component of the FFN network.

operation followed by a 3×3 conv layer. The up-sampling process involves a 3×3 ConvTransposed operation. Further details on the spatial-spectral prior learning branch and the low-rank prior learning branch will be provided subsequently.

Spatial Spectral Prior Learning Branch. A well designed proximal mapping module should adaptively learns HSI's local similarity and account for spectral nonlinear mapping. To achieve this, we propose SSPL to function as the feature extractor for both spatial and spectral dimensions. Fig. 3 (b) shows the SSPL used in the first level. SSPL consists of a spatial CNN and spectral self-attention. The spatial part with $conv3 \times 3$ and $Gelu$ can effectively extract local contextual information. The spectral part computes cross-covariance across feature channels, exploring the global characteristics of HSI to gives more weight to importance features.

Spectral self-attention follows [60]. The key component of spectral self-attention is presented in Fig. 3 (c). The input feature $X_{in} \in R^{H \times W \times C}$ is first embedded as Q , K , and V . Next, SSPL reshapes the query and key such that their dot-product interaction generates a transposed attention map

$A \in R^{C \times C}$. The SSPL process is defined as:

$$Attention(Q, K, V) = V \cdot Softmax\left(\frac{KQ}{\alpha}\right) \quad (6)$$

$$X_{SSPL} = W_p Attention(Q, K, V) \quad (7)$$

where $Q \in R^{HW \times C}$; $K \in R^{C \times HW}$; $V \in R^{HW \times C}$ are obtained after convolution and reshape operation from original size $\mathbb{R}^{H \times W \times C}$. α is a learnable scaling parameter to control the magnitude of the dot product K and Q before applying the softmax function.

Low-rank Prior Learning Branch. Low-rank representation of HSI can effectively maintain contextual relationships within high-dimensional structure. Several studies [61]–[64] have demonstrated its effectiveness for HSI tasks. To explore the spectral low-rank property of HSIs, [61] extended a deep CP Decomposition module to achieve low-rank prior learning. However, such a paradigm cannot learn optimal low-rank representation in deep unfolding network-based HSI reconstruction algorithms, since each deep prior network is independent, and the learned prior representation cannot be shared through stages. To address this challenge, we propose an inter-stages low-rank prior learning network.

The structure of low-rank prior learning module follows

[65], but the difference is that we share low-rank prior information between several stages as illustrated in Fig. 3 (b). Input features $X_{in} \in R^{H \times W \times C}$ are firstly mapped into a 1D tensor $L_c \in R^{1 \times 1 \times C}$ to aggregate global distribution in the spectral dimension. Then, it is projected into a subspace $L_k \in R^{1 \times 1 \times C/r}$ of rank C/r as follows:

$$L_c = \text{AveragePool}(X_{in}) \quad (8)$$

$$L_k = \text{Linear}(L_c) \quad (9)$$

To gather global spectral prior, a learnable query prior $Q_k \in R^{m \times C/r}$ interact with the squeezed feature L_k , and the output of low-rank prior learning module is obtained by rescaling the HSI $X_{in} \in R^{H \times W \times C}$ with informative low-rank attention $F_{atten} \in R^{1 \times m}$ as:

$$F_{atten} = \text{Softmax}\left(\frac{L_k Q_k^T}{\sqrt{C/r}}\right) \quad (10)$$

$$X_{LRPL} = X \cdot \text{Linear}(F_{atten} Q_k) \quad (11)$$

where \cdot denotes the element-wise dot product. In this module, the query prior function as an excitation to enhance the representation abilities of the squeezed feature, while the rescaling operation allows the current HSI to capture the low-rank prior of the entire HSI datasets.

Adaptive Feature Transfer Block. The encoder of U-Net acquires image's multi-scale detailed information from the image and gradually compresses the image size to capture global priors. The decoder then fuses up-sampled features with skip-connected features to progressively restore the image size. In this architecture, skip connections establish connections between the encoder and decoder, enabling the decoder to effectively utilize features from different levels and enhance the network's ability to preserve the details information. However, previous approaches that simply concatenate same scale encoder features of the same scale [28], [36] failed to adequately transfer useful information, while roughly fusing multi-scales encoder features [36] may introduce additional noise. Inspired by [66], we propose an adaptive feature transfer block that models multi-scale contextual correlation features using convolution-style attention, and then adaptively transfers them to decoder stage, adding only a small amount of computational overhead.

As presented in Fig.3 (d), the encoder feature $E_1 \in R^{H \times W \times C}$ and $E_2 \in R^{H \times W \times 2C}$ are processed through convolution operations to reduce the channel dimensionality and spatially down-sample E_1 , and to only reduce the channel dimensionality of E_2 :

$$E_{red}^1 = \text{Conv}(E_{in}^1) \quad (12)$$

$$E_{red}^2 = \text{Conv}(E_{in}^2) \quad (13)$$

After that, we utilize the product of the two-level features $E_{exc} \in R^{\frac{H}{2} \times \frac{W}{2} \times \frac{C}{2}}$ to draw attention to important feature co-existing in both, sum of them $E_{coe} \in R^{\frac{H}{2} \times \frac{W}{2} \times \frac{C}{2}}$ to integrate their exclusive feature. To fully integrate E_{exc} and E_{coe} , we use a 5×5 depth-wise convolution on their concatenation to

module contextual correlation attention as follows:

$$E_{exc} = E_{red}^1 \cdot E_{red}^2 \quad (14)$$

$$E_{coe} = E_{red}^1 + E_{red}^2 \quad (15)$$

$$E_{atten} = \text{DCConv}(E_{exc} \textcircled{C} E_{coe}) \quad (16)$$

where \textcircled{C} denotes the concatenation operation. Then, we further model multi-scales contextual correlation features with E_{atten} and process them into the original scale:

$$E_{con}^1 = \text{Up}(\text{Conv}(E_{atten} \cdot E_{red}^1)) \quad (17)$$

$$E_{con}^2 = \text{Conv}(E_{atten} \cdot E_{red}^2) \quad (18)$$

where $E_{con}^1 \in R^{H \times W \times C}$, $E_{con}^2 \in R^{\frac{H}{2} \times \frac{W}{2} \times 2C}$ are processed contextual correlation features. Finally, we fuse them with the origin encoder output such to transfer enriched detailed feature to the decoder:

$$E_{out}^1 = \text{Fusion}(E_{in}^1 \textcircled{C} E_{con}^1) \quad (19)$$

$$E_{out}^2 = \text{Fusion}(E_{in}^2 \textcircled{C} E_{con}^2) \quad (20)$$

where *Fusion* denotes the feature fusion block as presented in Fig 3. (e). The adaptive feature transfer network can collectively model multi-scale encoder features, thereby preventing the information loss when features are transferred level by level as in previous works.

IV. EXPERIMENTS

In this section, we compare our method with several state-of-the-art(SOTA) methods on the AVIRIS-NG(Airborne Visible InfraRed Imaging Spectrometer Next Generation) dataset. We selected 300 wavelengths ranging from 1000 *nm* to 2500 *nm* and removed the bands whose response values were zero due to water vapor absorption. The peak-signal-to-noise-ratio (PSNR) and structured similarity index metrics (SSIM) metrics are used to evaluate the performance of different hyperspectral image reconstruction methods.

A. Datasets

AVIRIS-NG measures the wavelengths ranging from 380 *nm* to 2510 *nm* with a 5 *nm* sampling interval. Spectra are captured as images with 600 cross-track elements and spatial sampling ranging from 0.3 m to 4.0 m. We selected 12 flight-lines, and each hyperspectral image is approximately sized at $21K \times 0.65K \times 432$. We create spatial domain tiles for each image, with each tile sized at $256 \times 256 \times 300$.

B. Implementation Details

Our model was implemented using the PyTorch framework and trained with the Adam optimizer for 300 epochs. During the training, we applied randomly cropping, rotation, and flipping of tiles for data augmentation. The learning rate was set to 2×10^{-4} and the batch size 1. The training and test data size was $64 \times 64 \times 300$. All experiments were conducted on the NVIDIA Tesla P40 GPU.

TABLE I
RESULTS ON 12 SIMULATED SCENES FROM AVIRIS-NG DATASET (SCENE 1 ~ SCENE 12). THE BEST RESULTS ARE IN BOLD.

Methods	scene 1	scene 2	scene 3	scene 4	scene 5	scene 6	scene 7	scene 8	scene 9	scene 10	scene 11	scene 12	average
TSANet	42.08	42.86	43.06	36.95	38.31	37.02	38.10	40.85	39.16	39.53	39.64	39.33	39.74
	0.990	0.992	0.993	0.971	0.975	0.970	0.981	0.990	0.987	0.985	0.986	0.984	0.984
ADMM-Net	42.26	43.63	43.81	37.65	38.84	37.77	37.87	40.73	39.35	39.56	39.58	39.36	40.03
	0.990	0.993	0.994	0.975	0.978	0.973	0.979	0.991	0.988	0.985	0.986	0.985	0.985
GAP-Net	42.30	43.74	43.91	37.60	38.87	37.85	37.85	40.78	39.46	39.52	39.52	39.27	40.06
	0.990	0.993	0.994	0.975	0.978	0.973	0.979	0.991	0.988	0.985	0.986	0.984	0.985
HDNet	42.71	44.50	44.49	39.35	40.33	39.69	39.26	41.77	39.97	40.12	40.20	40.21	41.05
	0.991	0.995	0.995	0.982	0.984	0.982	0.984	0.992	0.989	0.987	0.988	0.988	0.988
RDLUF	42.95	44.65	44.66	39.62	40.41	39.65	39.77	42.08	40.45	40.81	40.49	40.43	41.33
	0.991	0.994	0.994	0.983	0.984	0.980	0.985	0.991	0.989	0.988	0.989	0.988	0.988
Ours 3stage	38.12	40.67	39.99	36.88	37.37	33.16	37.22	38.37	38.15	38.75	38.93	39.10	38.06
	0.984	0.990	0.989	0.976	0.977	0.970	0.980	0.986	0.986	0.984	0.986	0.985	0.983
Ours 5stage	39.73	42.82	42.05	37.81	38.32	34.83	37.80	39.42	38.66	39.39	39.54	39.58	39.16
	0.984	0.991	0.990	0.978	0.978	0.970	0.980	0.986	0.986	0.984	0.986	0.986	0.983
Ours 7stage	43.23	44.80	44.71	39.06	39.99	39.04	39.27	42.17	40.23	40.53	40.68	40.64	41.20
	0.992	0.995	0.994	0.981	0.983	0.979	0.984	0.992	0.990	0.988	0.989	0.988	0.988
Ours 9stage	43.43	45.09	45.06	39.54	40.35	39.91	40.17	42.51	40.60	40.64	40.75	40.79	41.57
	0.992	0.995	0.995	0.983	0.984	0.982	0.987	0.992	0.990	0.988	0.990	0.989	0.989

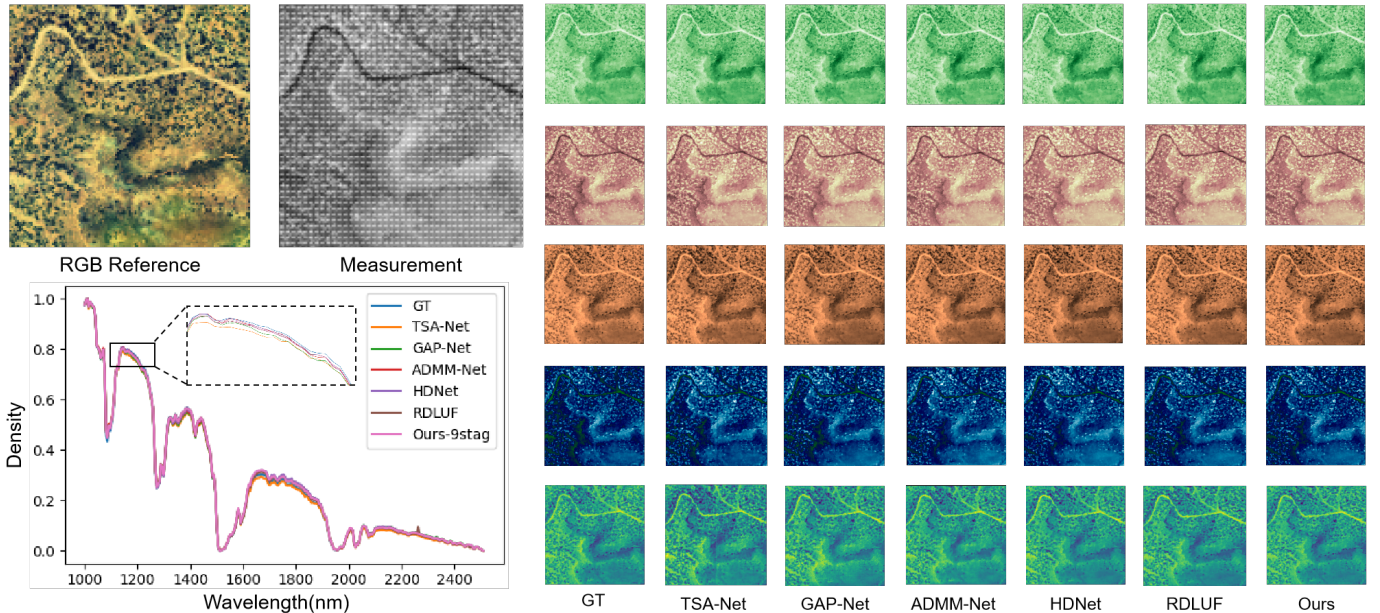


Fig. 4. Reconstruction results of our method and other reconstruction algorithms

C. Comparisons with SOTA Methods

We conducted a comprehensive comparative analysis of the proposed method and various SOTA methods, including two end-to-end methods (TSANet, HDNet) and three deep unfolding networks (GAP-Net, ADMM-Net, RDLUF). It is worth noting that RDLUF is implemented with help of the cross-stages interaction and multi-scales encoder feature fusion. We replaced the CASSI simulation imaging part of all comparison methods with the simulation process of filter array imaging,

adjusting the number of feature channels, and maintaining consistency in learning rate, loss function, optimizer settings as much as possible.

Table I presents 12 scenes and average results of PSNR and SSIM for the different comparison methods. Our method achieves best performance with both 41.57dB PSNR and 0.989 SSIM. TSANet learns both spatial and spectral correlations but shows the worst performance. Relative to the best counterpart method (RDLUF), another inter-stages feature learning

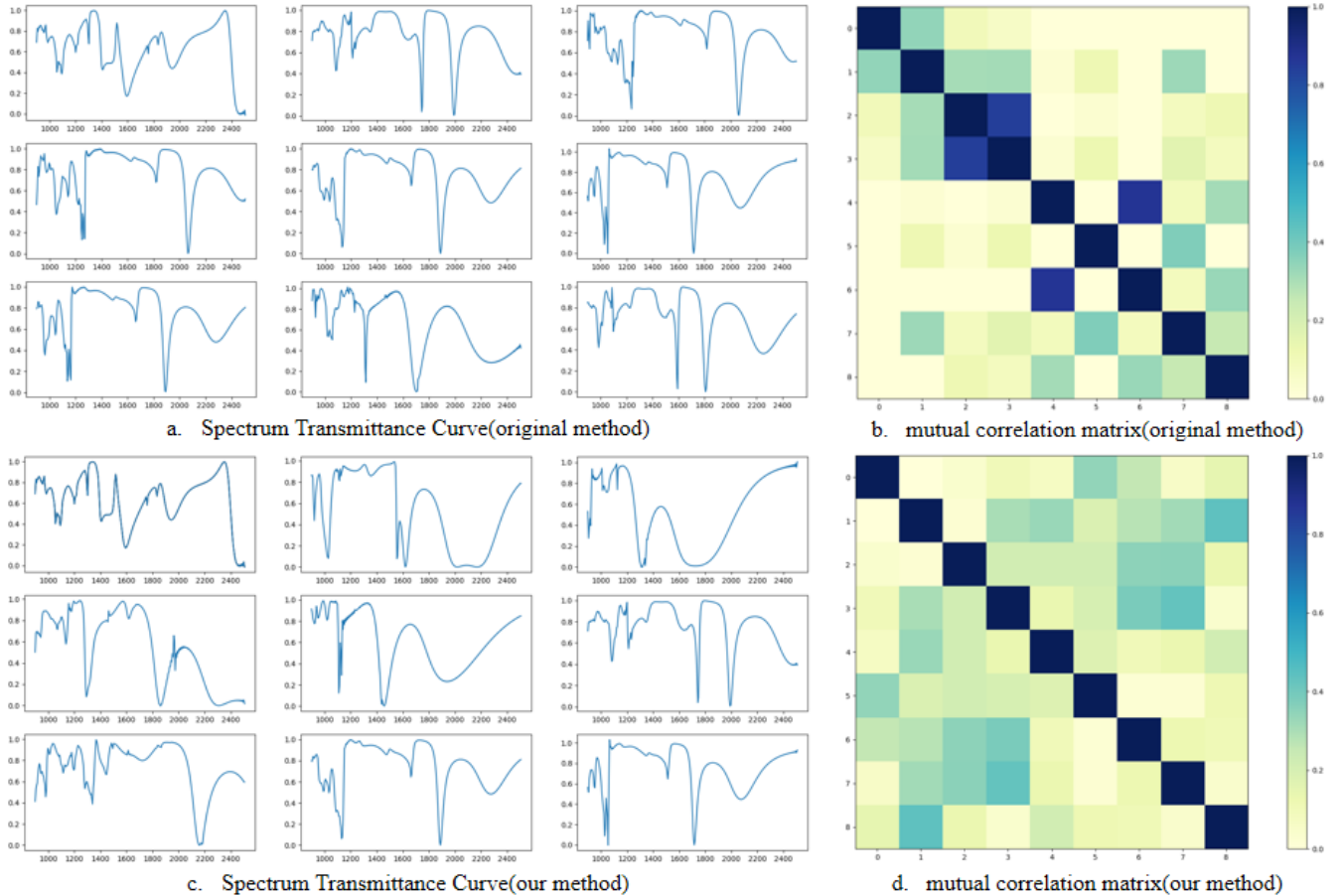


Fig. 5. Filter selection visual results of original and our methods

method, our method improves by an average of 0.24dB improvement in PSNR and a 0.001 improvement in SSIM. Different deep unfolding models(GAP-Net,ADMM-Net) simply uses a U-Net to learn the deep prior, without considering the inherent characteristics of HSI, leading to limited performance. HDNet presents results that are slightly lower than our method. Moreover, we find that model based method like DeSCI [18], GAP-TV [54] cannot resolve HSI reconstruction task on AVIRIS-NG dataset, we think that excessive number of bands and severe spectral variation result in this situation. In conclusion, the significant improvements show that the proposed method is effective for HSI reconstruction.

D. Ablation Study

We conducted ablation study to evaluate the effectiveness of various components of our proposed method.

Break-down Ablaton. We used a plain ISTA gradient descent module followed by a spatial-spectral prior learning(SSPL)-based U-Net as our baseline model. Subsequently, incorporating low-rank prior learning(LRPL) block to better extract global low rank prior information led to an improvement of 0.67dB. Adding a adaptive feature transfer(AFT) block to reduce feature loss between different scales, achieving an additional improvement of 0.44dB.

Number of stages. To explore the impact of the number K of stages, we analyze the variation of model performance ranging from 3 to 9 stages as presented in TABLE I. We find that the reconstruction quality improves with the increase in the number of stages, indicating the high efficiency of the iterative deep unfolding network design. However, the reconstruction quality improve slow down after nine stages. After weighing the balance between computational complexity and performance improvement, we set the number of stages to nine.

TABLE II
THE EFFECTIVENESS OF DIFFERENT COMPONENTS

	SSPL	LRPL	AFT
PSNR	40.46	41.13	41.57
SSIM	0.984	0.988	0.989
Paras	390.41M	455.57M	517.46M
GFLOPs	1124.81	1458.77	1561.29

V. CONCLUSION

In this paper, we enhance the Pearson correlation coefficient based filter selection and propose a inter and intra prior learning deep unfolding network for SWIR-HSI reconstruction. By integrating FPS into the original filter selection, we achieve

better optimization of filter arrays and higher reconstruction quality. To address the loss of detailed features in the network, a adaptive feature transfer module is introduced to adaptively fuse the detail information from encoder stages and transfer them to decoder stages. Experimental results demonstrate that our method outperforms previous HSI reconstruction network. **Limitations and social impact.** The proposed framework extends spectral filter array imager to SWIR wavelengths and contributes to the design of deep unfolding networks for other inverse problems. However, our framework currently cannot handle large-scale NIR-HSI due to the high number of bands involved.

REFERENCES

- [1] V. Backman, M. B. Wallace, L. Perelman, J. Arendt, R. Gurjar, M. Müller, Q. Zhang, G. Zonios, E. Kline, T. McGillican *et al.*, “Detection of preinvasive cancer cells,” *Nature*, vol. 406, no. 6791, pp. 35–36, 2000.
- [2] Z. Meng, M. Qiao, J. Ma, Z. Yu, K. Xu, and X. Yuan, “Snapshot multispectral endomicroscopy,” *Optics Letters*, vol. 45, no. 14, pp. 3897–3900, 2020.
- [3] Y.-Z. Feng and D.-W. Sun, “Application of hyperspectral imaging in food safety inspection and control: a review,” *Critical reviews in food science and nutrition*, vol. 52, no. 11, pp. 1039–1058, 2012.
- [4] J. M. Bioucas-Dias, A. Plaza, G. Camps-Valls, P. Scheunders, N. Nasrabadi, and J. Chanussot, “Hyperspectral remote sensing data analysis and future challenges,” *IEEE Geoscience and remote sensing magazine*, vol. 1, no. 2, pp. 6–36, 2013.
- [5] L. J. Williams, J. Cavender-Bares, P. A. Townsend, J. J. Couture, Z. Wang, A. Stefanski, C. Messier, and P. B. Reich, “Remote spectral detection of biodiversity effects on forest biomass,” *Nature Ecology & Evolution*, vol. 5, no. 1, pp. 46–54, 2021.
- [6] W. M. Porter and H. T. Enmark, “A system overview of the airborne visible/infrared imaging spectrometer (aviris),” in *Imaging spectroscopy II*, vol. 834. SPIE, 1987, pp. 22–31.
- [7] R. W. Basedow, D. C. Carmer, and M. E. Anderson, “Hydice system: Implementation and performance,” in *Imaging Spectrometry*, vol. 2480. SPIE, 1995, pp. 258–267.
- [8] N. Gat, “Imaging spectroscopy using tunable filters: a review,” *Wavelet Applications VII*, vol. 4056, pp. 50–64, 2000.
- [9] X. Hu, Y. Cai, J. Lin, H. Wang, X. Yuan, Y. Zhang, R. Timofte, and L. Van Gool, “Hdnet: High-resolution dual-domain learning for spectral compressive imaging,” in *Proceedings of the IEEE/CVF Conference on Computer Vision and Pattern Recognition*, 2022, pp. 17 542–17 551.
- [10] J. Lin, Y. Cai, X. Hu, H. Wang, X. Yuan, Y. Zhang, R. Timofte, and L. Van Gool, “Coarse-to-fine sparse transformer for hyperspectral image reconstruction,” in *European Conference on Computer Vision*. Springer, 2022, pp. 686–704.
- [11] Y. Cai, J. Lin, X. Hu, H. Wang, X. Yuan, Y. Zhang, R. Timofte, and L. Van Gool, “Mask-guided spectral-wise transformer for efficient hyperspectral image reconstruction,” in *Proceedings of the IEEE/CVF Conference on Computer Vision and Pattern Recognition*, 2022, pp. 17 502–17 511.
- [12] Z. Wang, S. Yi, A. Chen, M. Zhou, T. S. Luk, A. James, J. Nogan, W. Ross, G. Joe, A. Shahsafi *et al.*, “Single-shot on-chip spectral sensors based on photonic crystal slabs,” *Nature communications*, vol. 10, no. 1, p. 1020, 2019.
- [13] G. Cai, Y. Li, Y. Zhang, X. Jiang, Y. Chen, G. Qu, X. Zhang, S. Xiao, J. Han, S. Yu *et al.*, “Compact angle-resolved metasurface spectrometer,” *Nature Materials*, vol. 23, no. 1, pp. 71–78, 2024.
- [14] J. Xiong, X. Cai, K. Cui, Y. Huang, J. Yang, H. Zhu, W. Li, B. Hong, S. Rao, Z. Zheng *et al.*, “Dynamic brain spectrum acquired by a real-time ultraspectral imaging chip with reconfigurable metasurfaces,” *Optica*, vol. 9, no. 5, pp. 461–468, 2022.
- [15] H. He, Y. Zhang, Y. Shao, Y. Zhang, G. Geng, J. Li, X. Li, Y. Wang, L. Bian, J. Zhang *et al.*, “Meta-attention network based spectral reconstruction with snapshot near-infrared metasurface,” *Advanced Materials*, p. 2313357, 2024.
- [16] B. Arad and O. Ben-Shahar, “Filter selection for hyperspectral estimation,” in *Proceedings of the IEEE international conference on computer vision*, 2017, pp. 3153–3161.
- [17] J. M. Bioucas-Dias and M. A. Figueiredo, “A new twist: Two-step iterative shrinkage/thresholding algorithms for image restoration,” *IEEE Transactions on Image processing*, vol. 16, no. 12, pp. 2992–3004, 2007.
- [18] Y. Liu, X. Yuan, J. Suo, D. J. Brady, and Q. Dai, “Rank minimization for snapshot compressive imaging,” *IEEE transactions on pattern analysis and machine intelligence*, vol. 41, no. 12, pp. 2990–3006, 2018.
- [19] J. Tan, Y. Ma, H. Rueda, D. Baron, and G. R. Arce, “Compressive hyperspectral imaging via approximate message passing,” *IEEE Journal of Selected Topics in Signal Processing*, vol. 10, no. 2, pp. 389–401, 2015.
- [20] J. Yang, X. Yuan, X. Liao, P. Llull, D. J. Brady, G. Sapiro, and L. Carin, “Video compressive sensing using gaussian mixture models,” *IEEE Transactions on Image Processing*, vol. 23, no. 11, pp. 4863–4878, 2014.
- [21] Z. Meng, J. Ma, and X. Yuan, “End-to-end low cost compressive spectral imaging with spatial-spectral self-attention,” in *European conference on computer vision*. Springer, 2020, pp. 187–204.
- [22] Z. Shi, C. Chen, Z. Xiong, D. Liu, and F. Wu, “Hscnn+: Advanced cnn-based hyperspectral recovery from rgb images,” in *Proceedings of the IEEE Conference on Computer Vision and Pattern Recognition Workshops*, 2018, pp. 939–947.
- [23] X. Miao, X. Yuan, Y. Pu, and V. Athitsos, “l-net: Reconstruct hyperspectral images from a snapshot measurement,” in *Proceedings of the IEEE/CVF International Conference on Computer Vision*, 2019, pp. 4059–4069.
- [24] S. Zheng, Y. Liu, Z. Meng, M. Qiao, Z. Tong, X. Yang, S. Han, and X. Yuan, “Deep plug-and-play priors for spectral snapshot compressive imaging,” *Photonics Research*, vol. 9, no. 2, pp. B18–B29, 2021.
- [25] T. Huang, W. Dong, X. Yuan, J. Wu, and G. Shi, “Deep gaussian scale mixture prior for spectral compressive imaging,” in *Proceedings of the IEEE/CVF Conference on Computer Vision and Pattern Recognition*, 2021, pp. 16 216–16 225.
- [26] Y. Cai, J. Lin, H. Wang, X. Yuan, H. Ding, Y. Zhang, R. Timofte, and L. V. Gool, “Degradation-aware unfolding half-shuffle transformer for spectral compressive imaging,” *Advances in Neural Information Processing Systems*, vol. 35, pp. 37 749–37 761, 2022.
- [27] X. Zhang, Y. Zhang, R. Xiong, Q. Sun, and J. Zhang, “Herosnet: Hyperspectral explicable reconstruction and optimal sampling deep network for snapshot compressive imaging,” in *Proceedings of the IEEE/CVF Conference on Computer Vision and Pattern Recognition*, 2022, pp. 17 532–17 541.
- [28] J. Ma, X.-Y. Liu, Z. Shou, and X. Yuan, “Deep tensor admm-net for snapshot compressive imaging,” in *Proceedings of the IEEE/CVF International Conference on Computer Vision*, 2019, pp. 10 223–10 232.
- [29] Z. Meng, S. Jalali, and X. Yuan, “Gap-net for snapshot compressive imaging,” *arXiv preprint arXiv:2012.08364*, 2020.
- [30] Y. Dong, D. Gao, T. Qiu, Y. Li, M. Yang, and G. Shi, “Residual degradation learning unfolding framework with mixing priors across spectral and spatial for compressive spectral imaging,” in *Proceedings of the IEEE/CVF Conference on Computer Vision and Pattern Recognition*, 2023, pp. 22 262–22 271.
- [31] L. Wang, C. Sun, M. Zhang, Y. Fu, and H. Huang, “Dnu: Deep non-local unrolling for computational spectral imaging,” in *Proceedings of the IEEE/CVF Conference on Computer Vision and Pattern Recognition*, 2020, pp. 1661–1671.
- [32] S. Zhang, L. Wang, L. Zhang, and H. Huang, “Learning tensor low-rank prior for hyperspectral image reconstruction,” in *Proceedings of the IEEE/CVF Conference on Computer Vision and Pattern Recognition*, 2021, pp. 12 006–12 015.
- [33] T. Huang, X. Yuan, W. Dong, J. Wu, and G. Shi, “Deep gaussian scale mixture prior for image reconstruction,” *IEEE Transactions on Pattern Analysis and Machine Intelligence*, 2023.
- [34] X. Chen, J. Yang, and L. Xiao, “Learning deep subspace projection prior for dual-camera compressive hyperspectral imaging,” *IEEE Geoscience and Remote Sensing Letters*, vol. 19, pp. 1–5, 2022.
- [35] L. Wang, Z. Wu, Y. Zhong, and X. Yuan, “Snapshot spectral compressive imaging reconstruction using convolution and contextual transformer,” *Photonics Research*, vol. 10, no. 8, pp. 1848–1858, 2022.
- [36] Y. Dong, D. Gao, T. Qiu, Y. Li, M. Yang, and G. Shi, “Residual degradation learning unfolding framework with mixing priors across spectral and spatial for compressive spectral imaging,” in *Proceedings of the IEEE/CVF Conference on Computer Vision and Pattern Recognition*, 2023, pp. 22 262–22 271.
- [37] J. M. Bioucas-Dias and M. A. Figueiredo, “A new twist: Two-step iterative shrinkage/thresholding algorithms for image restoration,” *IEEE Transactions on Image processing*, vol. 16, no. 12, pp. 2992–3004, 2007.

- [38] M. Aharon, M. Elad, and A. Bruckstein, "K-svd: An algorithm for designing overcomplete dictionaries for sparse representation," *IEEE Transactions on signal processing*, vol. 54, no. 11, pp. 4311–4322, 2006.
- [39] X. Yuan, T.-H. Tsai, R. Zhu, P. Llull, D. Brady, and L. Carin, "Compressive hyperspectral imaging with side information," *IEEE Journal of selected topics in Signal Processing*, vol. 9, no. 6, pp. 964–976, 2015.
- [40] W. He, N. Yokoya, and X. Yuan, "Fast hyperspectral image recovery of dual-camera compressive hyperspectral imaging via non-iterative subspace-based fusion," *IEEE Transactions on Image Processing*, vol. 30, pp. 7170–7183, 2021.
- [41] Y. Liu, X. Yuan, J. Suo, D. J. Brady, and Q. Dai, "Rank minimization for snapshot compressive imaging," *IEEE transactions on pattern analysis and machine intelligence*, vol. 41, no. 12, pp. 2990–3006, 2018.
- [42] J. Yang, X. Liao, X. Yuan, P. Llull, D. J. Brady, G. Sapiro, and L. Carin, "Compressive sensing by learning a gaussian mixture model from measurements," *IEEE Transactions on Image Processing*, vol. 24, no. 1, pp. 106–119, 2014.
- [43] C.-C. Chang and H.-N. Lee, "On the estimation of target spectrum for filter-array based spectrometers," *Optics Express*, vol. 16, no. 2, pp. 1056–1061, 2008.
- [44] S. Zhang, Y. Dong, H. Fu, S.-L. Huang, and L. Zhang, "A spectral reconstruction algorithm of miniature spectrometer based on sparse optimization and dictionary learning," *Sensors*, vol. 18, no. 2, p. 644, 2018.
- [45] A. Robles-Kelly, "Single image spectral reconstruction for multimedia applications," in *Proceedings of the 23rd ACM international conference on Multimedia*, 2015, pp. 251–260.
- [46] T. Stiebel, S. Koppers, P. Seltsam, and D. Merhof, "Reconstructing spectral images from rgb-images using a convolutional neural network," in *Proceedings of the IEEE Conference on Computer Vision and Pattern Recognition Workshops*, 2018, pp. 948–953.
- [47] O. Ronneberger, P. Fischer, and T. Brox, "U-net: Convolutional networks for biomedical image segmentation," in *Medical image computing and computer-assisted intervention—MICCAI 2015: 18th international conference, Munich, Germany, October 5-9, 2015, proceedings, part III 18*. Springer, 2015, pp. 234–241.
- [48] Y. B. Can and R. Timofte, "An efficient cnn for spectral reconstruction from rgb images," *arXiv preprint arXiv:1804.04647*, 2018.
- [49] Y. Zhao, L.-M. Po, Q. Yan, W. Liu, and T. Lin, "Hierarchical regression network for spectral reconstruction from rgb images," in *Proceedings of the IEEE/CVF Conference on Computer Vision and Pattern Recognition Workshops*, 2020, pp. 422–423.
- [50] Z. Cheng, B. Chen, R. Lu, Z. Wang, H. Zhang, Z. Meng, and X. Yuan, "Recurrent neural networks for snapshot compressive imaging," *IEEE Transactions on Pattern Analysis and Machine Intelligence*, vol. 45, no. 2, pp. 2264–2281, 2022.
- [51] R. He, W.-S. Zheng, T. Tan, and Z. Sun, "Half-quadratic-based iterative minimization for robust sparse representation," *IEEE transactions on pattern analysis and machine intelligence*, vol. 36, no. 2, pp. 261–275, 2013.
- [52] S. Boyd, N. Parikh, E. Chu, B. Peleato, J. Eckstein *et al.*, "Distributed optimization and statistical learning via the alternating direction method of multipliers," *Foundations and Trends® in Machine learning*, vol. 3, no. 1, pp. 1–122, 2011.
- [53] A. Beck and M. Teboulle, "A fast iterative shrinkage-thresholding algorithm for linear inverse problems," *SIAM journal on imaging sciences*, vol. 2, no. 1, pp. 183–202, 2009.
- [54] X. Yuan, "Generalized alternating projection based total variation minimization for compressive sensing," in *2016 IEEE International conference on image processing (ICIP)*. IEEE, 2016, pp. 2539–2543.
- [55] X. Yuan, Y. Liu, J. Suo, and Q. Dai, "Plug-and-play algorithms for large-scale snapshot compressive imaging," in *Proceedings of the IEEE/CVF Conference on Computer Vision and Pattern Recognition*, 2020, pp. 1447–1457.
- [56] S. Zheng, Y. Liu, Z. Meng, M. Qiao, Z. Tong, X. Yang, S. Han, and X. Yuan, "Deep plug-and-play priors for spectral snapshot compressive imaging," *Photonics Research*, vol. 9, no. 2, pp. B18–B29, 2021.
- [57] L. Wang, C. Sun, Y. Fu, M. H. Kim, and H. Huang, "Hyperspectral image reconstruction using a deep spatial-spectral prior," in *Proceedings of the IEEE/CVF Conference on Computer Vision and Pattern Recognition*, 2019, pp. 8032–8041.
- [58] J. Chung, C. Gulcehre, K. Cho, and Y. Bengio, "Empirical evaluation of gated recurrent neural networks on sequence modeling," *arXiv preprint arXiv:1412.3555*, 2014.
- [59] J. Song, C. Mou, S. Wang, S. Ma, and J. Zhang, "Optimization-inspired cross-attention transformer for compressive sensing," in *Proceedings of the IEEE/CVF Conference on Computer Vision and Pattern Recognition*, 2023, pp. 6174–6184.
- [60] S. W. Zamir, A. Arora, S. Khan, M. Hayat, F. S. Khan, and M.-H. Yang, "Restormer: Efficient transformer for high-resolution image restoration," in *Proceedings of the IEEE/CVF conference on computer vision and pattern recognition*, 2022, pp. 5728–5739.
- [61] S. Zhang, L. Wang, L. Zhang, and H. Huang, "Learning tensor low-rank prior for hyperspectral image reconstruction," in *Proceedings of the IEEE/CVF Conference on Computer Vision and Pattern Recognition*, 2021, pp. 12006–12015.
- [62] Y. Chang, L. Yan, and S. Zhong, "Hyper-laplacian regularized unidirectional low-rank tensor recovery for multispectral image denoising," in *Proceedings of the IEEE Conference on Computer Vision and Pattern Recognition*, 2017, pp. 4260–4268.
- [63] W. Dong, G. Shi, X. Li, Y. Ma, and F. Huang, "Compressive sensing via nonlocal low-rank regularization," *IEEE transactions on image processing*, vol. 23, no. 8, pp. 3618–3632, 2014.
- [64] J. Huang, T.-Z. Huang, L.-J. Deng, and X.-L. Zhao, "Joint-sparse-blocks and low-rank representation for hyperspectral unmixing," *IEEE Transactions on Geoscience and Remote Sensing*, vol. 57, no. 4, pp. 2419–2438, 2018.
- [65] J. Hu, L. Shen, and G. Sun, "Squeeze-and-excitation networks," in *Proceedings of the IEEE conference on computer vision and pattern recognition*, 2018, pp. 7132–7141.
- [66] Q. Hou, C.-Z. Lu, M.-M. Cheng, and J. Feng, "Conv2former: A simple transformer-style convnet for visual recognition," *IEEE Transactions on Pattern Analysis and Machine Intelligence*, 2024.